Fatigue Fract. Engng Mater. Struct. Vol. 20, No. 1, pp. 49–60, 1997
Printed in Great Britain.

8756-758X/97 $6.00 + 0.00

INTERFACIAL CRACK INITIATION UNDER QUASI-STATIC AND DYNAMIC LOADING CONDITIONS: AN EXPERIMENTAL STUDY

H. V. TIPPUR and L. XU
Department of Mechanical Engineering, 202 Ross Hall, Auburn University, Auburn, Alabama 36849

Received in final form 7 September 1996

Abstract—Interfacial fracture parameters under quasi-static and dynamic loading are examined in a large elastic mismatch bimaterial system. A wide range of remote field loading ratios of shear and tension are considered. The crack tip fields are mapped using the optical method of coherent gradient sensing or CGS and fracture parameters are quantified. Distinctly different crack initiation responses are observed for positive and negative shear stresses acting on the interface. Also, low velocity impact loading experiments are conducted to study the influence of dynamic loading on crack initiation parameters. Dynamic interfacial crack tip fields are recorded using high speed photography and fracture parameters for dynamically loaded stationary cracks are obtained. Measurements suggest significant crack initiation toughness reduction under dynamic loading conditions.

Keywords—Interfacial cracks; Shearing interferometry; Crack tip fields; Static and dynamic fracture toughness.

NOMENCLATURE

$a, \hat{a}$ = crack length and characteristic length
B = specimen thickness
c = elasto-optic constant
c_{lp}, c_{sp}, c_R = longitudinal, shear and Rayleigh wave speeds for PMMA
E_1, E_2 = complex amplitude distribution
k = wave number $(=2\pi/\lambda)$
K = complex stress intensity factor $(=K_1 + iK_2)$
$\mathcal{N}, \mathcal{M}$ = fringe orders
p, Δ = grating pitch and separation distance
P = applied load
r, ϕ = crack tip polar coordinates
s = off-set distance
W, C, D, L = specimen dimensions
x, y = crack tip Cartesian coordinates
ε = oscillation index
θ, λ = diffraction angle, wave length
Θ = applied load mixity
ν, μ = Poisson's ratio, shear modulus
$\psi(a), \hat{\psi}(\hat{a})$ = mode-mixity

INTRODUCTION

Bimaterial systems with large stiffness mismatch are encountered in composite materials, adhesive joints, microelectronic devices, and so on. The mechanical integrity of such systems depend on the failure characteristics of weak interfaces. A framework for analyzing dissimilar material interface fracture has been worked out in recent years based on the so-called oscillatory singularity first presented by Williams [1], and subsequently enriched by many others. The state-of-the-art was reviewed by Rice [2] and Hutchinson and Suo [3] for quasi-static problems. Dynamic failure

characteristics of interfacial systems are at the present relatively unexplored. Willis [4] predicted interfacial crack propagation speeds slightly in excess of the lower of the two Rayleigh wave speeds in bimaterials. Recently, dynamic optical measurements in polymermetal bimaterial systems by Tippur and Rosakis [5] suggested crack speeds of about 80% of the Rayleigh wave speed of the polymer. Further research is reported by Yang *et al.* [6], on steady-state elastodynamic fields for isotropic material joints, Wu [7] on anisotropic bimaterial joints and Liu *et al.* [8], on transient higher order stress fields for isotropic bimaterial joints with first time experimental evidence of intersonic crack speeds in polymermetal systems, have continued to shed light on this topic.

Here we present results pertaining to both quasi-static and dynamic crack initiation near isotropic bimaterial interfaces. First, interfacial crack tip fracture parameters were evaluated over a wide range of applied load mixities under quasi-static conditions using bimaterial specimens made of PMMA and aluminum. Crack tip parameters were obtained by full-field, optical measurements using coherent gradient sensing (CGS). Secondly, experimental results dealing with dynamic crack initiation due to stress wave loading were investigated in the same bimaterial system by examining the time history of fracture parameters leading to crack initiation.

COHERENT GRADIENT SENSING (CGS)

In this investigation the optical method of transmission CGS was used for mapping the crack tip deformations. The optical arrangement for transmission CGS is shown in Fig. 1. The working principle of the method is as follows: A collimated laser beam is transmitted through a phase object in the region of interest. Subsequently, the object wave front undergoes a series of diffraction as it propagates through two Ronchi rulings G_1 and G_2 of pitch p (lines parallel to, say, x-axis). The two grating planes are parallel and are separated by distance Δ along the optical axis. The

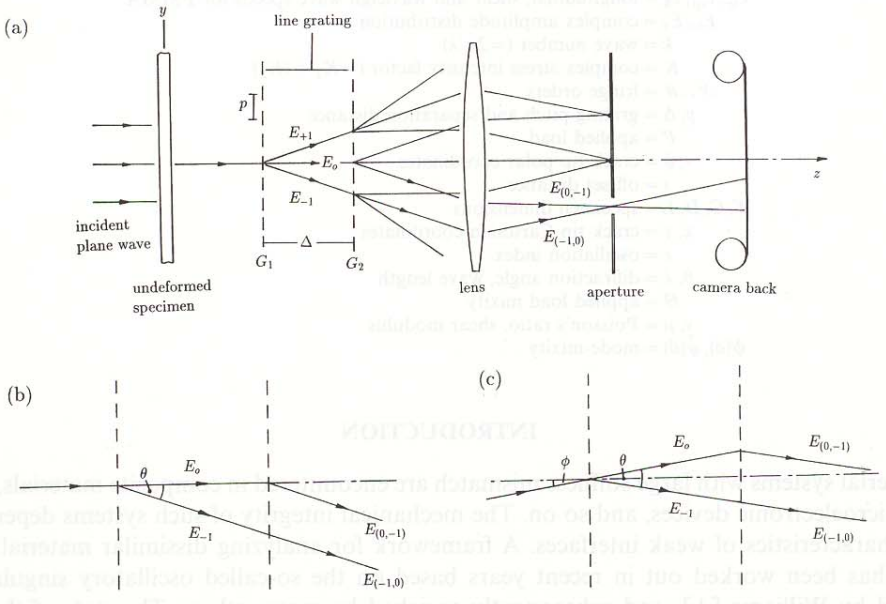

Fig. 1. Working principle of transmission CGS: (a) Schematic of the optical set-up. (b) Wavefront shearing for undeformed object. (c) Wavefront shearing for deformed object.

square wave transmission profile of the gratings ($p = 25\ \mu$m and $\Delta = 30$–70 mm have produced satisfactory results) result in zero and several odd diffraction orders. Here, for simplicity diffraction orders E_0, E_{+1} and E_{-1} only are considered and θ is the diffraction angle ($\theta \approx (\lambda/p)$). The diffracted wave fronts emerging from the grating G_2 are collected by the lens and spatial filtering is performed by blocking all but $+1$ or -1 diffraction orders as shown. The filtered information produces laterally sheared object wave fronts on the image plane. Note that the recording arrangement consisting of the filtering lens and the camera back combinations is focussed on the object plane. Initially optics is aligned to get a uniform bright field on the image plane when the object is undeformed. Upon deformation light rays are deflected from the initial propagation direction parallel to the optical axis due to a combination of stress-optic and Poisson effects near the crack tip. For transmission CGS, it has been shown through detailed analyses [9,10] that stress field induced wave front warpage can be related to in-plane gradients of $(\sigma_x + \sigma_y)$ where σ_x, σ_y are the normal thickness average stresses components:

$$cB\frac{\partial(\sigma_x + \sigma_y)}{\partial y} = \frac{\mathcal{N}p}{\Delta}, \quad cB\frac{\partial(\sigma_x + \sigma_y)}{\partial x} = \frac{\mathcal{M}p}{\Delta}. \tag{1}$$

In the above c is the elasto-optic constant for the planar phase object, $\mathcal{M}$, $\mathcal{N}$ $(=0, \pm1, \pm2, \ldots)$ are fringe orders, and B is the nominal thickness of the specimen.

QUASI-STATIC INTERFACIAL FAILURE

Bimaterial specimens

A model material combination with a large stiffness mismatch between PMMA and aluminum was chosen (Young's modulus ratio $E_1 : E_2 = 1 : 24$ and Poisson ratio $\nu_1 : \nu_2 = 0.35 : 0.3$). The test specimens were made from two equal thickness ($B = 6$ mm) halves joined by methyl-methacrylate monomer and a polymerizing agent. A thin Teflon tape insert was used to produce a sharp edge discontinuity of length $a/W = 0.33$ along the interface where a $(= 25$ mm) and W denote the crack length and the specimen height, respectively. The bond was cured at room temperature prior to testing. The resulting post-cure thickness of the bond material was approximately 50–100 μm. Before testing, each specimen was optically examined in the CGS set-up under no-load condition to ensure a residual stress-free interface.

Experiments and fringe analysis

Asymmetric four-point-bend bimaterial specimens were used in this study to obtain a wide range of mode-mixities. The specimen and loading configurations are shown in Fig. 2. The specimens were loaded in a displacement controlled loading device and the applied load P was measured. Different far field mixities were introduced by varying the loading off-set distance s between the interface and the loading axis (see Fig. 2). Note that when $s = 0$, the crack plane is under pure shear and increasing values of s result in increasing bending moment (opening) acting on the crack plane for the same magnitude of shear force when C and D are unchanged. Experiments were conducted for both "positive" s and "negative" s values ($+s$ and $-s$ arrangements produce positive and negative shear on the crack plane, respectively; Fig. 2 corresponds to "negative" s shear). Other relevant test parameters were $C/W = 1.27$ and $D/W = 0.63$. The average shear and maximum normal stress acting on the crack plane for the configuration are given by, $\tau = P(C - D)/WB(C + D)$, $\sigma = 6\tau s/W$. From the above, a measure of applied load mixity on the crack plane can be introduced as $\Theta = \tan^{-1}(\tau/\sigma) = \tan^{-1}(W/6s)$. Here, Θ is dependent on the eccentricity ratio (s/W) and is independent of C and D.

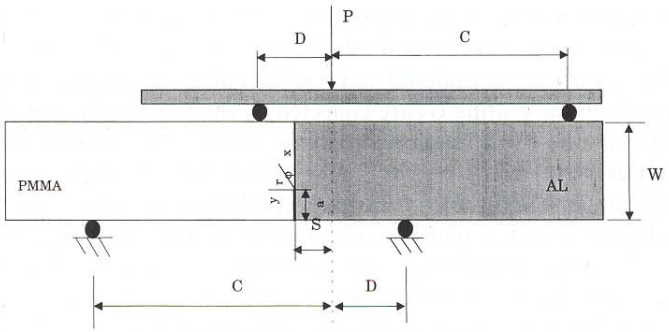

Fig. 2. Asymmetric four-point-bend fracture specimen.

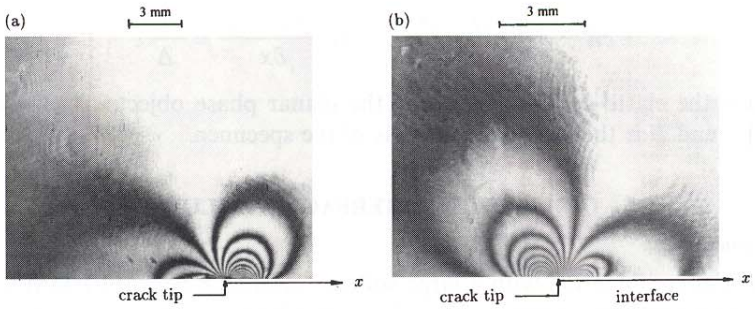

Fig. 3. Typical CGS fringes (contours of $(\sigma_x + \sigma_y)_{,x}$), (a) $s/W = -0$, (b) $s/W = +0.33$.

The resulting interference patterns obtained using CGS represent contours of $(\sigma_x + \sigma_y)_{,x}$ in the PMMA half in approximately $4B$ radius semicircular region near the crack tip. The interference patterns were recorded for s/W ratios varying from -0.5 to 0.5. Typical interference patterns for two different values of $s/W = -0$ and $+0.33$ are shown in Fig. 3. An angular deflection of 0.028° of light results in a fringe.

Considering the material above the interface ($0 < \phi < \pi$), and following Rice [2], the asymptotic expression for CGS fringes can be derived as given below:

$$cB\frac{\partial(\sigma_x+\sigma_y)}{\partial x} = 4cB\Bigg(\sum_{n=1,3,5,\ldots}^{\infty} e^{\varepsilon(\phi-\pi)} r^{((n/2)-2)} \times \left\{A_n\left[\left(\frac{n}{2}-1\right)\cos\left(\left(\frac{n}{2}-2\right)\phi-\varepsilon\ln(r/a)\right)+\varepsilon\sin\left(\left(\frac{n}{2}-2\right)\phi-\varepsilon\ln(r/a)\right)\right]\right.$$
$$\left. + B_n\left[\left(\frac{n}{2}-1\right)\sin\left(\left(\frac{n}{2}-2\right)\phi-\varepsilon\ln(r/a)\right)-\varepsilon\cos\left(\left(\frac{n}{2}-2\right)\phi-\varepsilon\ln(r/a)\right)\right]\right\}$$
$$+\sum_{n=2,4,6,\ldots}^{\infty}\frac{c_2}{c_1+c_2}nr^{((n/2)-1)}\left[A_n\cos\left(\frac{n}{2}-1\right)\phi+B_n\sin\left(\frac{n}{2}-1\right)\phi\right]\Bigg)=\frac{\mathscr{M}p}{\Delta} \quad (2)$$

where $c_i = (\kappa_i + 1)/\mu_i$, $\kappa_i = (3 - \nu_i)/(1 + \nu_i)$ for plane stress ($i = 1$ for PMMA and $= 2$ for aluminum), $\mathscr{M} = 0, \pm 1, \pm 2 \ldots$ denote fringe orders and (r, ϕ) are crack tip polar coordinates. Here μ and ν

represent the shear modulus and Poisson's ratio respectively, and ε is,

$$\varepsilon = \frac{1}{2\pi} \ln \frac{\mu_1 + \mu_2 \kappa_1}{\mu_2 + \mu_1 \kappa_2}.$$

For PMMA-aluminum interface $\varepsilon = 0.098$ for plane stress. In the above expression, the complex stress intensity factor is given by, $(Ka^{i\varepsilon}) = 2\sqrt{2\pi}\cosh(\pi\varepsilon)(A_1 + iB_1)$. When contributions from the higher order terms ($n > 1$ in Eq. (2)) are negligible compared to the dominant $n = 1$ term, the above equation assumes its K-dominant form. The mode-mixity is, $\psi(a) = \tan^{-1} \mathrm{Im}(Ka^{i\varepsilon})/\mathrm{Re}(Ka^{i\varepsilon})$ and mixity based on a different length $\hat{a}$ can be calculated using $\hat{\psi}(\hat{a}) = \psi + \varepsilon \log((\hat{a})/a)$.

The fringe patterns were digitized and fringe location (r, ϕ) and fringe order $(\mathcal{M})$ in the near tip region all around the crack tip were measured. Recognizing the existence of a region of dominant 3D deformations near the crack tip [11] data in the region ($r/B \geqslant 0.5$, $30° \leqslant \phi \leqslant 150°$) near the crack tip was used in the analysis. To extract stress intensity factors from fringe patterns, overdeterministic least-squares data analyses were performed. In the analysis K-dominant assumptions were relaxed and higher order terms were incorporated sequentially in order to account for possible non-singular contributions to the field at distances beyond the anticipated 3-D zone. The procedure consists of minimizing a function $\Phi(r, \phi; A_1, B_1, A_2, B_2, \ldots) = \Sigma_{i=1}^{M} w_i[F_i - F_i^{exp}]^2$, with respect to the constants A_n and B_n. Here F and F^{exp} are the right hand sides in Eq. (2), M denote the total number of data points used in the analysis and w_i are the weighting factors.

A complementary finite element analysis was also carried out using ABAQUS™ software package and asymmetric bimaterial specimen geometry described earlier. The finite element model consisted of 1016 eight node plane stress elements and 3235 nodes. The crack tip region was discretized using a fine mesh with crack tip elements as small as $0.015a$, a being the crack length. The parameter $a/W = 0.33$ was kept constant while s/W was varied in the range of $-0.5 \leqslant s/W \leqslant 0.5$. The finite element counterparts of $\mathrm{Re}(Ka^{i\varepsilon})$, $\mathrm{Im}(Ka^{i\varepsilon})$ and hence crack tip mixity ψ were obtained using the interaction energy release rate method [12] while the domain integral method was used for calculating different path independent integrals. These results are reported in detail elsewhere [13].

Crack tip parameters

Measured crack tip parameter ψ is compared with its finite element counterpart in Fig. 4(a) in the range $-0.5 \leqslant s/W \leqslant 0.5$. The measurements (filled circles for "negative" set-up and filled boxes for "positive" set-up) are in good agreement with the finite element results for both "positive" and "negative" set-up. In the range $+0 \leqslant s/W \leqslant 0.04$ when the applied load is dominated by shear, the measured and the computed values of crack tip mixity exceed $\pi/2$ because of a negative $\mathrm{Re}(Ka^{i\varepsilon})$ and positive $\mathrm{Im}(Ka^{i\varepsilon})$. As s/W increases (positive set-up) ψ steadily decreases to approximately 20° at large s/W. On the contrary, mixity corresponding to negative shear is approximately $-55°$ at $s/W = -0$ and approaches 0° at large s/W. For the range of experimental parameters used in the study applied mixity Θ varies from approximately $\pm 18°$ to $\pm 90°$. In Fig. 4(b), crack tip mixity ψ is plotted as a function of applied mixity Θ and a linear relationship ($\psi = m_0\Theta + \psi_0$) between the two is evident. These crack tip measurements demonstrate a simple phase shift between interfacial crack tip mixity and the applied load mixity. Although such phase shifts are suggested [3] for small ε to simplify the physical interpretation of interface stress intensity factors analogous to homogeneous counterparts, this result demonstrates of the same even when ε is very large. The broken line represents a straight line fit through the data whose slope m_0 is approximately equal to 1 and the intercept $\psi_0 \approx 18°$. Note that ψ_0 is dependent on the material mismatch parameters nd length scale which in this investigation is taken to be crack length a. The observed linearity

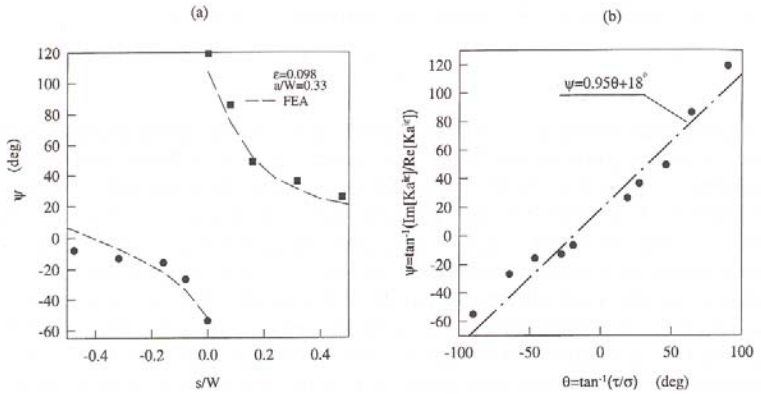

Fig. 4. Applied and crack tip mode-mixities in asymmetric four-point-bending bimaterial specimens. (a) Variation of crack tip mixity with s/W. (b) Variation of crack tip mixity with applied mixity.

suggests that if an alternative length scale $\hat{a} \approx 1.0 \times 10^{-3}$ m is chosen instead of the current choice of $a = 25 \times 10^{-3}$ m, it would make the crack tip mixity coincide with the applied load mixity, i.e., $\hat{\psi} = \Theta$ where $\hat{\psi} = \psi + \varepsilon \ln(\hat{a}/a)$.

Interfacial fracture strength and toughness

Next several failure tests were conducted using specimens bonded in "as-machined" condition (surface roughness $R_a \approx 1.5\ \mu$m for aluminum). The tests were conducted at a constant cross-head displacement rate of 50 mm/min. Specimens were loaded for different s/W ratios ranging from -0.5 to 0.5. Several specimens were tested at each s/W ratio. In each case, the peak load was recorded as P_{cr} corresponding to crack initiation. Note that P_{cr} is related to crack initiation toughness in this specimen configuration as $\mathrm{Re}(K\hat{a}^{i\varepsilon}) \propto f_1(s/W)P\sqrt{a}$ and $\mathrm{Im}(K\hat{a}^{i\varepsilon}) \propto f_2(s/W)P\sqrt{a}$. Explicit relations of the same can be found in O'Dowd *et al.* [14]. A typical P_{cr} vs. s/W curve is shown in Fig. 5(a) where the filled boxes correspond to the "positive" set-up while filled circles correspond to the "negative" set-up (the broken lines only suggest data trends). Note that these data reflect only the ones corresponding to interfacial fracture between the two materials and all data corresponding to interlayer fracture of the adhesive is dropped from further analysis (in-layer fracture is particularly prevalent when the imposed shear is positive). Evidently P_{cr} values depend on whether the crack plane shear is positive or negative in this bimaterial system. The value of P_{cr} is higher for $s/W = -0$ when compared with the one for $s/W = +0$ (by a factor of about 1.5). The difference in P_{cr} values between $s/W = -0$ and $+0$ is due to the crack tip interpenetration when the crack tip is subjected to dominant negative shear loading. A theoretical study of the same for frictionless crack surfaces has been reported by Comninou and Schmueser [15] for interfacial cracks experiencing different combinations of normal and shear tractions. The P_{cr} data along with the crack tip mixity presented earlier was used next for calculating the crack initiation toughness K_{cr} ($= |Ka^{i\varepsilon}|$). Plot of K_{cr} vs. $\hat{\psi}$ is shown in Fig. 5(b). When the applied shear is negative, the observed trends are similar to those reported by Wang and Suo [16], Liechti and Chai [17], O'Dowd *et al.* [18], and Tippur and Ramaswamy [19]. (Note that oscillation index $\varepsilon < 0$ in other studies while $\varepsilon > 0$ here.) K_{cr} values generally increase at larger negative mixities. On the whole, K_{cr} vs. $\hat{\psi}$ is asymmetric about $\hat{\psi} = 0$ and for this bimaterial system

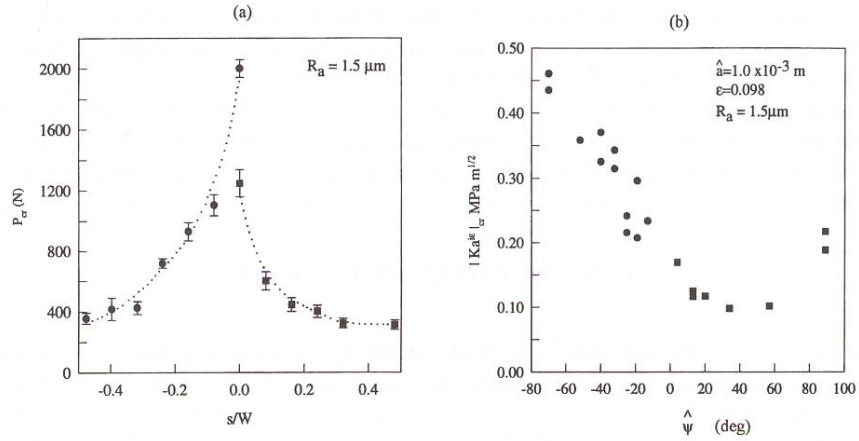

Fig. 5. Fracture strength and crack initiation toughness for as-machined surfaces: (a) fracture strength vs. s/W, (b) crack initiation toughness vs. crack tip mixity.

the smallest value of toughness is in the range of $30° < \hat{\psi} < 60°$. The crack initiation toughness shows an increasing trend at large values of positive $\hat{\psi}$. Although the overall variation in the $K_{cr}(\hat{\psi})$ is similar to the one obtained by Liechti and Chai [17], toughness values for dominant positive shear are much lower than the ones for negative shear acting on the interface. In their study of the infuence of plasticity on interfacial fracture toughness, Tvergaard and Hutchinson [20] predict a behavior similar to the one shown in Fig. 5(b). Asymmetries like the one observed here are predicted when relative tangential displacements near the crack are effectively suppressed in the fracture process zone (see Fig. 8(b) in [20]). In Fig. 6 crack initiation strength and toughness data corresponding to a higher surface roughness (sand blast surface: $R_a = 4.5$ μm) of the edges of the specimen prior to bonding. Note that the increased surface roughness has led to higher fracture strength (see Fig. 6(a)). Again, the sense of the applied shear seems to result in different failure strengths. It should be mentioned that, however, inlayer fracture could not be avoided over most

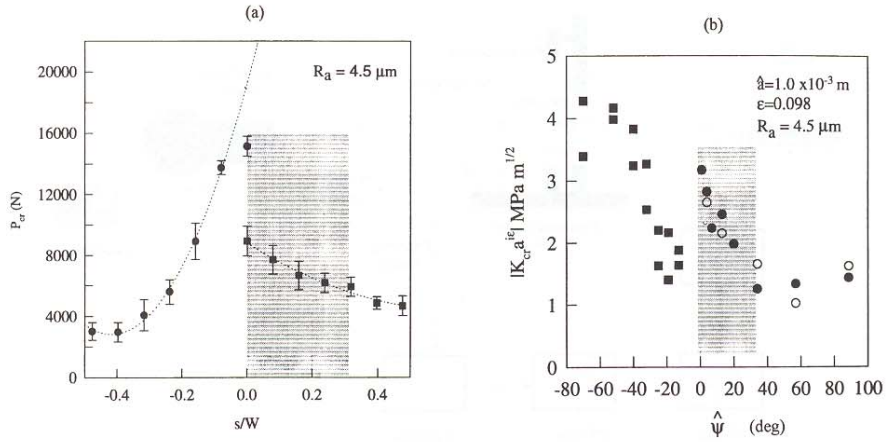

Fig. 6. Fracture strength and crack initiation toughness for sand blasted surfaces: (a) fracture strength vs. s/W, (b) crack initiation toughness vs. crack tip mixity.

of the s/W values for positive shear cases. The inlayer failure data correspond to the s/W values shown in the shaded region. Hence, the K_{cr} plot shows a "spike" in the neighborhood of $\hat{\psi} = 0$ in Fig. 6(b) (values corresponding to the shaded region). Outside this region, the variation of toughness curve is similar to that of the as-machined surface discussed in Fig. 5(b). Evidently, the increase in roughness by a factor of 3 seems to have resulted in a fracture strength (and fracture toughness) multiplied by 3^2. Further experimentation is necessary to confirm this speculation that crack initiation toughness varies as a square of the surface roughness parameter R_a.

DYNAMIC INTERFACIAL FAILURE

Experiments

Next, evolution of interfacial crack tip fields under stress wave loading was examined using CGS. The experiments were conducted with the same bimaterial system described earlier. The bimaterial models were subjected to low velocity impact loading (tup velocity of approximately 3.5 m/s) in a three-point-bending configuration using a pneumatic linear thruster. Note that in these experiments specimens with height $W = 50$ mm, crack length $a = 12.5$ mm ($a/W = 0.25$) were used. The distance between the supports L was varied during the experiments in order to simulate crack initiation under different mode-mixities. In the first set of experiments L/W ratios of 5.6, 3.6, 2.6, and 2.0 were considered with impact location at 12.5 mm away from the interface on the PMMA to aluminum side. In the second set of experiments L/W ratios of 5.6, 3.6, 2.6 were used with impact location at 12.5 mm away from the interface on the aluminum side of the bimaterial specimen.

The dynamic experimental set-up (see Fig. 7) consisted of the CGS interferometer used in conjunction with an Argon-ion pulse laser as the light source and a high speed camera for recording the interference pattern. A framing rate of 185,000 fps (50 ns pulses, 5.5 μs repetition rate) was used for capturing the evolution of crack tip stress fields upon impact. The experimental procedure used in these experiments was as follows: A coaxially mounted three face mirror, attached to a compressed air driven turbine shaft, was first brought to speed. A steel impactor was then pneumatically launched towards the specimen. A photodetector triggered the camera shutter "open" a few milliseconds before the tup made contact with the specimen. Upon contact (time,

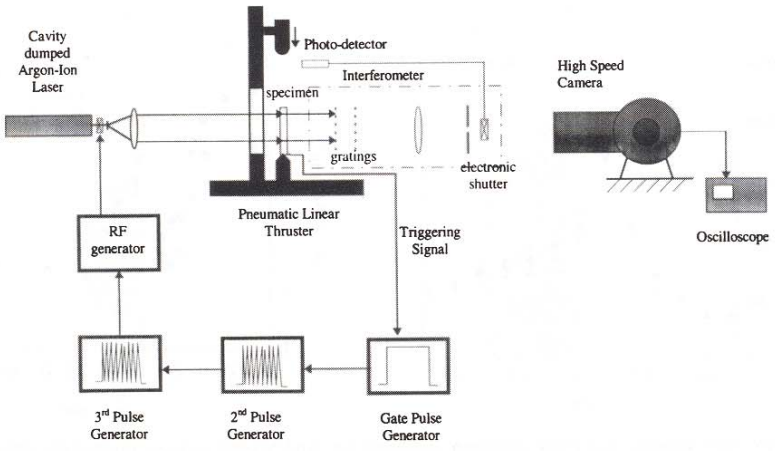

Fig. 7. Schematic for measuring dynamic interfacial fracture toughness.

$t = 0$), a trigger pulse initiated a gated string of laser pulses, at a present repetition rate and duration, lasting a third of the period of the turbine shaft rotation. A strip of 35 mm 400 ASA Kodak T-Max film, residing in the high speed camera film track over a 240° arc of a circle, captured discrete "frozen" images of the interference in a 50 mm semicircular region.

Fringe analysis and dynamic fracture parameters

In these experiments we have examined transient crack tip fields during impact loading. In Fig. 8, a few representative interference patterns of $\partial(\sigma_x + \sigma_y)/\partial x$ contours from a recorded sequence are shown. The time $t = 0$ corresponds to the time when the impactor makes contact with the specimen. The fringes correspond to the situation when the PMMA side (approximately 12.5 mm away from the interface) of the interface was impacted with a velocity of 3.5 m/s. Here, we were able to map interference patterns resulting from the deformations at the impact location as well as the crack tip, simultaneously. The interference patterns corresponding to the loading point on the PMMA half of the specimen are evident near the top edge of the specimen. As seen, with time these fringes grow in size suggesting a rapid increase in the load at the impact point, and resemble the quasi-static counterparts [19]. In these experiments, the fringe evolution at the crack tip is evident approximately 50 μs after impact suggesting a time delay after the stress waves are launched into the specimen (the longitudinal and shear wave speeds for PMMA are: $c_{lp} = 2080$ m/s, $c_{sp} = 1000$ m/s). These interference patterns were used for extracting the transient load and the fracture parameters leading up to crack initiation and propagation. Using the appropriate field equations for a line load acting on the edge of an elastic half-space, the transient load at the point of impact was extracted. The impact load is plotted as a function of t in Fig. 9(a). Note that the load history is essentially a ramp loading with disturbances at approximately 50 and 100 μs corresponding to wave reflections reaching the impact location after the initial contact. The sudden drop in the load record indicates crack initiation event. By assuming an average ramp loading, the loading rate can

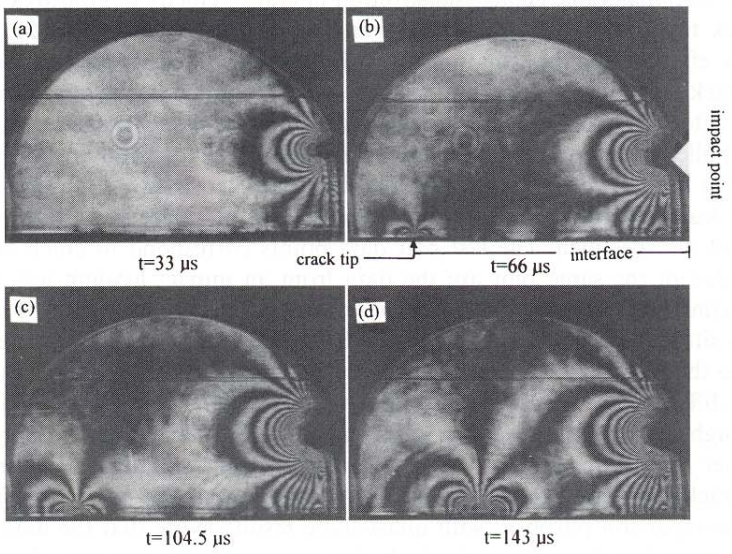

Fig. 8. Selected transient interfacial crack tip fringes (impact velocity 3.5 m/s, $L/W = 5.6$, and 0.02°/fringe) from a sequence (framing rate 185,000 frames per second). First two frames: pre-initiation fringes, last two frames: post-initiation fringes.

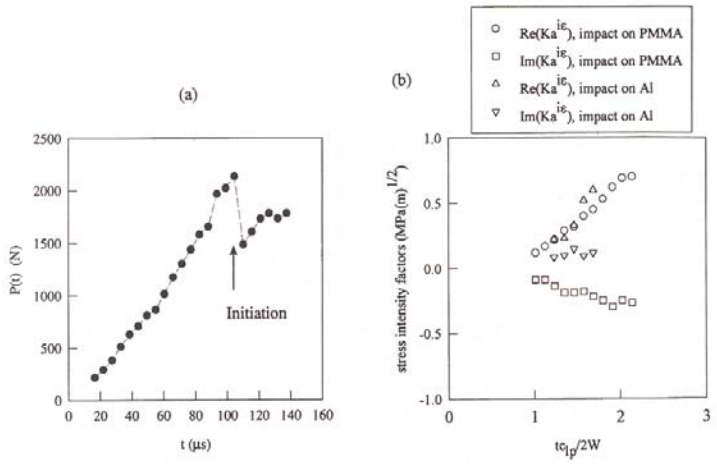

Fig. 9. Optical measurements from CGS fringes: (a) Impact loading history (impact on PMMA, $L/W = 5.6$). (b) Stress intensity factor history.

be estimated to be in the range of 17–20 MN/sec. It should also be noted that the dynamic load reported here are only estimates since we have used the solutions of a dynamic load acting on an elastic homogeneous half-space. However, the presence of aluminum provides a stiffer material response and hence the estimated values are bound to underestimate the true load.

In this work, we are interested in the events leading up to crack initiation (dynamically loaded stationary crack) in bimaterials. Hence, substitution of crack velocity $\dot{a} \to 0$ provides simplification of dynamic crack tip fields in Yang *et al.* [6], and assume the form of Eq. (2) discussed earlier and the dynamic effects enter the equation through the stress intensity factors. Hence, estimation procedure for crack tip parameters is similar to the one elaborated in the quasi-static case and the dynamic effects enter the equation through the complex stress intensity factor. Figure 9(b) shows (filled circles and filled boxes) a plot of dynamic stress intensity factor estimates vs. non-dimensional time $\hat{t} = (tc_{1p}/2W)$ for $L/W = 5.6$ and using the dominant terms ($n = 1$ in Eq. (2)) as the basis functions in the least-squares analysis. Kinks seen in these plots are due to the wave reflections from the edges of the specimen. The last pair data points correspond to crack initiation in each case. Also included in the same plot are the data from an impact loading test wherein the tup impacts the specimen on the aluminum side of the interface at a distance of 12.5 mm from the interface. In this situation, the crack tip stress intensity factor $\mathrm{Re}(Ka)^{ie}$ matches well with the ones corresponding to the impact on the PMMA side. However, the crack initiation values of $\mathrm{Im}(Ka)^{ie}$ are significantly different for both situations. Note that the results here correspond to a roughened (sandblasted; roughness parameter $R_a = 4.5\ \mu$m) surface prior to bonding. Similar results are also obtained for other L/W ratios and are discussed in detail elsewhere [21]. A summary of fracture parameters at crack initiation are shown in Fig. 10. Here, the mode-mixity ($\hat{\psi}(\hat{a})$) is scaled using $\hat{a} = 0.001$ m for comparison purposes with quasi-static results. Note that the data under dynamic conditions are somewhat limited (particularly for positive mode-mixities) due to the current restrictions in our experimental set-up. The fracture toughness variations are similar to the quasi-static counterparts shown in Fig. 6(b). The crack initiation toughness increases with increasing

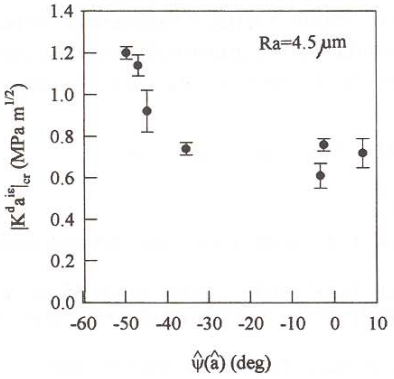

Fig. 10. Dynamic crack initiation toughness for PMMA-aluminum interfaces.

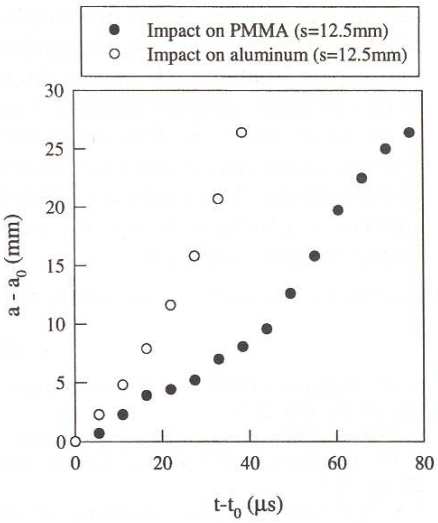

Fig. 11. Crack growth history.

(magnitude) mode-mixity from approximately $0.6\,\mathrm{MPa}\sqrt{\mathrm{m}}$ at $\hat{\psi}(\hat{a}) \approx -3°$ to $1.2\,\mathrm{MPa}\sqrt{\mathrm{m}}$ at $\hat{\psi}(\hat{a}) \approx -52°$. These values, when compared with the quasi-static counterparts, suggest a significant fracture toughness reduction by a factor of at least 2 for impact loading conditions for this bimaterial interface. In Fig. 11 (t_0 = time at crack initiation) crack growth history is recorded for the two impact situations discussed above. Evidently, the crack propagation event is highly transient in both the cases with maximum instantaneous crack speeds of $0.72c_R$ (Rayleigh wave speed c_R for PMMA = 970 m/s) and $1.1c_R$. Also the crack speed observed for the case of impact on the aluminum side corresponds to intersonic speed (between the shear wave and longitudinal wave speeds) for PMMA and is consistent with the observations of Liu *et al.* [8].

CONCLUSIONS

Some conclusions of this work are as follows:

(1) Optical measurements of crack tip fields using the method of coherent gradient sensing has been carried out over a wide range of far-field mode-mixities using asymmetric four-point-bend PMMA-aluminum bimaterial specimens. The applied mixity and the crack tip mixity are related through a simple phase shift. Failure load tests indicate that interfacial fracture toughness has a strong dependence on mode-mixity, the sense of the applied shear on the interface, and surface roughness. The fracture strength of the interface for pure positive shear is lower by a factor of approximately 1.5 when compared to the pure negative shear counterpart. Consequently, the fracture toughness curves show asymmetry attributed to the sign of the applied shear on the interface. Between the extreme values of toughness an approximate four fold change in the toughness is evident. Most importantly, the lowest value of the fracture toughness occurs at some combination of tensile and shear stresses acting in the far-field.

(2) Impact loading experiments have been conducted on the PMMA-aluminum bimaterials to investigate dynamic interfacial crack tip fields. These experiments use a coherent gradient

sensing technique in conjunction with high speed imaging at speeds of 185,000 frames per second for stress field mapping. The bimaterial specimens are subjected to low velocity impact loading, and impact location and support distances are varied between experiments to produce crack initiation under different dynamic loading conditions. Crack tip stress fields are mapped in real-time to study the fracture parameter history in different cases up to crack initiation. Fracture parameters at crack initiation are measured to obtain fracture toughness as a function of mode-mixity. The toughness values show trends similar to the quasi-static experiments but significant reductions in fracture toughness, at least by a factor of two, are evident under impact loading conditions.

Acknowledgments—The support for this work by NSF (Grant MSS-9313153) is gratefully appreciated.

REFERENCES

1. M. L. Williams (1959) The stresses around a fault or crack in dissimilar media. *Bul. Seismological Soc. Am.* **49**(2), 199–203.
2. J. R. Rice (1988) Elastic fracture mechanics concepts for interfacial cracks. *J. Appl. Mech.* **55,** 98–103.
3. J. W. Hutchinson and Z. Suo (1991) Mixed-mode cracking in layered materials. *Adv. Appl. Mech.* **29,** 63–191.
4. J. R. Willis (1971) Fracture mechanics of interfacial cracks. *J. Mech. Phys. Solids* **19,** 353–368.
5. H. V. Tippur and A. J. Rosakis (1991) Quasi-static and dynamic crack growth along bimaterial interfaces: A note on crack tip field measurements using coherent gradient sensing. *Exp. Mech.* **31**(3), 243–252.
6. W. Yang, Z. Suo and C. F. Shih (1991) Mechanics of dynamic debonding. *Proc. Royal Soc. London A* **433,** 679–697.
7. K. C. Wu (1991) Explicit crack tip fields for stationary and steadily growing interface cracks in anisotropic bimaterials. *Int. J. Solids. Struct.* **27**(4), 455–466.
8. C. Liu, J. Lambros and A.J. Rosakis (1993) Highly transient elastodynamic crack growth in a bimaterial interface: Higher order asymptotic analysis and optical experiments. *J. Mech. Phys. Solids* **41,** 1887–1954.
9. H. V. Tippur (1992) Coherent gradient sensing: A Fourier optics analysis and applications to fracture. *Applied Optics* **31**(22), 4428–4439.
10. H. V. Tippur, S. Krishnaswamy and A. J. Rosakis (1991) Optical mapping of crack tip deformations using the method of transmission and reflection coherent gradient sensing: A study of crack tip *K*-dominance. *Int. J. Fract.* **52,** 91–117.
11. Y. J. Lee and A. J. Rosakis (1993) Interfacial cracks in plates: Three dimensional numerical investigation. *Int. J. Solids Struct.* **30**(22), 3139–3158.
12. C. F. Shih and R. J. Asara (1988). Elastic–plastic analysis of cracks on bimaterial interfaces: Part 1, small scale yielding. *J. Appl. Mech.* **55,** 299–316.
13. L. Xu and H. V. Tippur (1995) Fracture properties for interfacial cracks: An experimental-finite element study of crack tip fields and crack initiation toughness. *Int. J. Fract.* **71,** 345–363.
14. M. Comninou and D. Schmueser (1979) The interface crack. *J. Appl. Mech.* **46,** 345–348.
15. N. P. O'Dowd, C. F. Shih and M. G. Stout (1992a) Test geometries for measuring interfacial fracture toughness. *Int. J. Solids Struct.* **29,** 571–589.
16. J.-S. Wang and Z. Suo (1990) Experimental determination of interfacial toughness curves using Brazil-nut-sandwiches. *Acta Metallurgica* **38**(7), 1279–1290.
17. K. M. Liechti and Y. S. Chai (1991) Biaxial loading experiments for determining interfacial fracture toughness. *J. Appl. Mech.* **58,** 680–687.
18. N. P. O'Dowd, M. G. Stout and C. F. Shih (1992b) Fracture toughness of alumina–niobium interfaces: Experiments and analyses. *Phil. Mag. A* **66**(6), 1037–1064.
19. H. V. Tippur and S. Ramaswamy (1993) Measurement of mixed-mode fracture parameters near cracks in homogeneous and bimaterial beams. *Int. J. Fract.* **61,** 247–265.
20. V. Tvergaard and J. W. Hutchinson (1993) The influence of plasticity on mixed-mode interface toughness. *J. Mech. Phys. Solids* **41**(6), 1119–1135.
21. L. Xu (1996) Investigation of interfacial crack tip fields and fracture toughness under quasi-static and dynamic loading conditions, Ph.D. Dissertation, Auburn University, Alabama.